# Overview of the ASPIRE Project's Supersonic Flight Tests of a Strengthened DGB Parachute

Clara O'Farrell
Jet Propulsion Laboratory
California Institute of Technology
Pasadena, CA 91109
818-354-8497
Clara.O'Farrell@jpl.nasa.gov

Bryan S. Sonneveldt
Jet Propulsion Laboratory
California Institute of Technology
Pasadena, CA 91109
818-354-3192
Bryan.S.Sonneveldt@jpl.nasa.gov

Chris Karlgaard
AMA Inc.
NASA Langley Research Center
Hampton, VA 23681
757-864-2178
Chris.Karlgaard-1@nasa.gov

Jake A. Tynis
AMA Inc.
NASA Langley Research Center
Hampton, VA 23681
757-864-3044
Jake.A.Tynis@nasa.gov

Ian G. Clark
Jet Propulsion Laboratory
California Institute of Technology
Pasadena, CA 91109
818-354-0535
Ian.G.Clark@jpl.nasa.gov

*Abstract*— The Advanced Supersonic Parachute Inflation Research Experiments (ASPIRE) project is aimed at developing and exercising a capability for testing supersonic parachutes at Mars-relevant conditions. The initial flights for ASPIRE were targeted as a risk-reduction activity for NASA's upcoming Mars2020 mission. For this effort, two candidate Disk-Gap-Band (DGB) parachute designs were tested at Mach number and dynamic pressure conditions relevant to Mars2020. The two parachutes under investigation were a build-to-print version of the DGB used by the Mars Science Laboratory and a strengthened version of this parachute that has the same geometry but differs in materials and construction. The first flight test (SR01) of the build-to-print parachute took place on October 4, 2017, followed by the first test of the strengthened parachute during flight SR02 on March 31, 2018. A second test of the strengthened parachute with a higher target load, SR03, took place on September 7, 2018. During the SR02 test, a Terrier-Black Brant sounding rocket delivered a payload containing the packed 21.5-m parachute, the deployment mortar, and the ASPIRE instrumentation suite to a peak altitude of 54.8 km. As the payload descended back towards the Atlantic Ocean the strengthened parachute was mortar-deployed at a Mach number of 1.97 and a dynamic pressure of 670 Pa, and produced a peak load of 55.8 klbf. During the SR03 flight, the strengthened parachute was deployed from an identical test platform at a Mach number of 1.85 and a dynamic pressure of 932 Pa, and produced a peak force of 67.4 klbf. This paper describes ASPIRE's two sounding rocket flight tests of the strengthened parachute: SR02 and SR03. It provides an overview of flight operations, test conditions, the data acquired during testing, the techniques used for post-flight reconstruction, and the reconstructed performance of the test vehicle and parachute system for each flight.

## TABLE OF CONTENTS

## 1. INTRODUCTION

The supersonic Disk-Gap-Band (DGB) parachute was developed during a series of campaigns undertaken by NASA in the 1960's and 1970's for the Viking project [1]. These campaigns included wind tunnel testing [2], [3], [4], low altitude drop testing [5], and high-altitude supersonic parachute testing [6], [7], [8]. Following the successful landing of the Viking spacecraft in 1976, every United States mission to the Martian surface has used a variant of the Viking DGB: 1997's Mars Pathfinder [9], [10], the Mars Polar Lander two years later [11], the twin Mars Exploration Rovers in 2004 [12], the Phoenix lander in 2007 [13], 2012's Mars Science Laboratory (MSL) [14], and the InSight lander in November 2018 [15]. Several modifications were made to the Viking DGB design in response to technological improvements and in response to mission-specific requirements. While these missions conducted subscale development tests and subsonic low-altitude qualification tests, none of the DGBs used since Viking were tested supersonically before their use on Mars. Instead, previous missions have relied on heritage data from the Viking qualification.

*The ASPIRE Project*

The Advanced Supersonic Parachute Inflation Research Experiments (ASPIRE) project was begun in 2016 to develop a capability for testing supersonic parachutes at Mars-relevant conditions using a sounding rocket test platform. The initial series of ASPIRE flights was focused on testing candidate parachute designs for the Mars2020 project [16]. During the first sounding rocket test, SR01, a build-to-print version of the MSL DGB was deployed at conditions similar to those MSL encountered at Mars: a Mach number of 1.77 and a dynamic pressure of 452 Pa [17]. During the two tests that followed, SR02 and SR03, a strengthened version of the MSL parachute that has the same geometry but differs in materials and construction was tested at loads higher than those experienced by the MSL DGB at Mars.

This paper describes the ASPIRE project's two tests of the strengthened DGB parachute, which took place on March 31 and September 7 of 2018. Figure 1 shows the concept of operations for SR02 and SR03. The test articles were delivered to targeted deployment conditions representative of flight at Mars by NASA's Sounding Rocket Operations Contract (NSROC) sounding rockets. The sounding rocket assembly, consisting of a Terrier first stage, a Black Brant

second stage, and the roughly 1200 kg payload section containing the experiment, were launched out of NASA's Wallops Flight Facility (WFF). The system was rail-launched and spin-stabilized at ~4 Hz. During flight, the first and second stages burned out at altitudes of approximately 1 km and 16 km respectively. The payload section reached an apogee altitude of 54.8 km on SR02 and 48.8 km on SR03 before beginning the descent to the Atlantic Ocean. When the payload reached the target dynamic pressure ($q_\infty$) and Mach number conditions, the parachute was mortar-deployed. The target conditions at trigger were Mach 1.72 and 532 Pa on SR02, and Mach 1.72 and 780 Pa on SR03.

In both flights, the parachute was deployed successfully and sustained no significant damage. The deployment, inflation, and supersonic and subsonic aerodynamics of the parachute were analyzed by a suite of instruments including: a three-camera high-speed/high-resolution stereographic video system trained on the parachute, situational awareness video cameras, a set of load pins at the interface of the parachute triple-bridle and the payload, and a GPS and inertial measurement unit (IMU) onboard the payload. After decelerating to subsonic speed, the parachute and payload descended to the ocean, were they were recovered and inspected and the required test data was collected.

The paper is organized as follows. The ASPIRE sounding rocket test platform, test articles, and onboard and range instrumentation suite are described in Section 2. Section 3 discusses mission operations, including launch, flight, and recovery. The atmosphere and test conditions on the day of launch are described in Section 4, while the performance of the strengthened parachute in these conditions is discussed in Section 5. Finally, concluding remarks and avenues for future work are described in Section 6. The results presented in this paper correspond to version 4.2 of the ASPIRE SR02 reconstructed trajectory, and version 4.0 of the SR03 reconstructed trajectory.

## 2. TEST ARCHITECTURE

*Test Platform*

Figure 2 shows a schematic of the ASPIRE configuration prior to launch from WFF. The payload section had a maximum diameter of 0.72 m and was 7.54 m in length. It was comprised of a nose cone ballast section that was jettisoned before splashdown; a section housing electronics and foam for buoyancy; a telemetry section housing the S-band telemetry equipment, GPS antennas, and C-band transponder; a section housing the attitude control system (ACS) including the inertial measurement unit (IMU); and the experiment section containing the parachute mortar tube and ASPIRE instrumentation. The payload also included an aft-transition section that remained attached to the Brant motor at separation. On SR02, the mass of the payload after separating from the Black Brant (including the stowed parachute and 602 kg nose cone) was 1201 kg. On SR03, additional ballast was added to the the payload in order to increase the dynamic pressure at parachute deploy. The SR03 payload had a total mass after Black Brant separation of 1277 kg, including the 676 kg nose cone.

*Test Articles*

The strengthened parachute tested on SR02 and SR03 was an 80-gore DGB with a design nominal diameter ($D_0$) of 21.45 m. The design and as-built dimensions of the SR02

and SR03 test articles are listed in Table 1. The geometry of the strengthened canopy was identical to that of the MSL DGB that was tested in SR01, but higher-strength materials were used in its construction [16]. The broadcloth gores were constructed using a Nylon fabric built to a custom specification by Heathcoat Fabrics. The 1.9 oz/yd$^2$ fabric had a rated strength of 110 lbf/in and a nominal air permeability of 80 ft$^3$/min/ft$^2$. The circumferential reinforcements at the trailing edge of the disk and the band leading and trailing edges were 2400 lbf Kevlar webbing. The reinforcements at the vent were 6000 lbf Kevlar webbing. The parachute was built using a continuous line construction where the suspension lines continued in to the canopy as the radials, crossed the vent and continued along the opposite side of the canopy. The radials/suspension lines were constructed from 3200 lbf Technora line. The canopy was attached to the aft end of the payload by means of a 7.8-m-long riser and a triple bridle. The entire packed parachute assembly had a mass of 85 kg (29 kg more than the MSL parachute pack).

Figure 3 shows a schematic of the ASPIRE configuration after parachute deploy. The relevant dimensions of the parachute-payload system are labeled in the schematic, and their values are listed in Table 1. Note that the parachute was tested in the wake of a slender payload whose diameter is approximately one sixth of the 4.5 m aeroshell housing the payload for the MSL and Mars2020 missions.

**Table 1**. **Dimensions of the ASPIRE parachute system.**

| Item | Symbol | Design | SR02 | SR03 |
|---|---|---|---|---|
| Parachute ref diameter (m) | $D_0$ | 21.45 | 21.50 | 21.55 |
| Parachute ref area (m$^2$) | $S_0$ | 361.36 | 363.16 | 364.62 |
| Vent diameter (m) | $D_V$ | 1.50 | 1.51 | 1.52 |
| Disk diameter (m) | $D_D$ | 15.62 | 15.60 | 15.64 |
| Gap height (m) | $H_G$ | 0.90 | 0.9 0 | 0.90 |
| Band height (m) | $H_B$ | 2.60 | 2.59 | 2.60 |
| Geometric porosity | $\lambda_g$ | 12.8% | 12.7% | 12.7% |
| Suspension line length (m) | $L_S$ | 36.47 | 36.53 | 36.52 |
| Riser length (m) | $L_R$ | 7.78 | 7.79 | 7.79 |
| Bridle length (m) | $L_B$ | 1.30 | - | - |
| Forebody diameter (m) | $d$ | 0.72 | 0.72 | 0.72 |

*Instrumentation*

The ASPIRE payload was equipped with scientific instrumentation to measure the trajectory, aerodynamics, and performance of the test vehicle and test article. Additional instrumentation not discussed in this paper provided diagnostic information on the payload and its electrical systems, such as temperature or voltage information. A summary of the onboard instrumentation is provided in Table 2.

*NIACS*— A NSROC Inertial Attitude Control System (NI-ACS) was located on the ACS section of the payload. The NIACS consists of a gimbaled LN-200 with miniature airborne computer (GLN-MAC) and a set of cold-gas thrusters. The single gimbal on the GLN-MAC was approximately aligned with the roll axis of the vehicle, thus allowing the LN-200 IMU to record the acceleration and angular rate of the payload at a rate of 400 Hz even during the spinning powered phase. An optical resolver on the GLN-MAC allows measurement of the gimbal angle at 400 Hz. A set of four cold-gas thrusters located at 90 deg intervals around the circumference of the experiment section was used to maintain
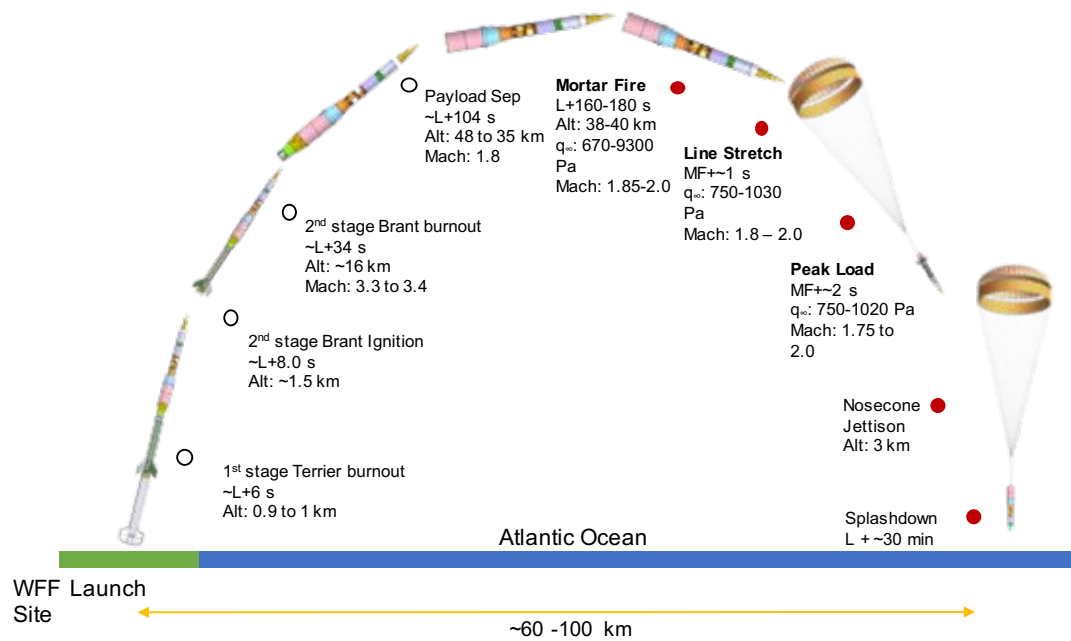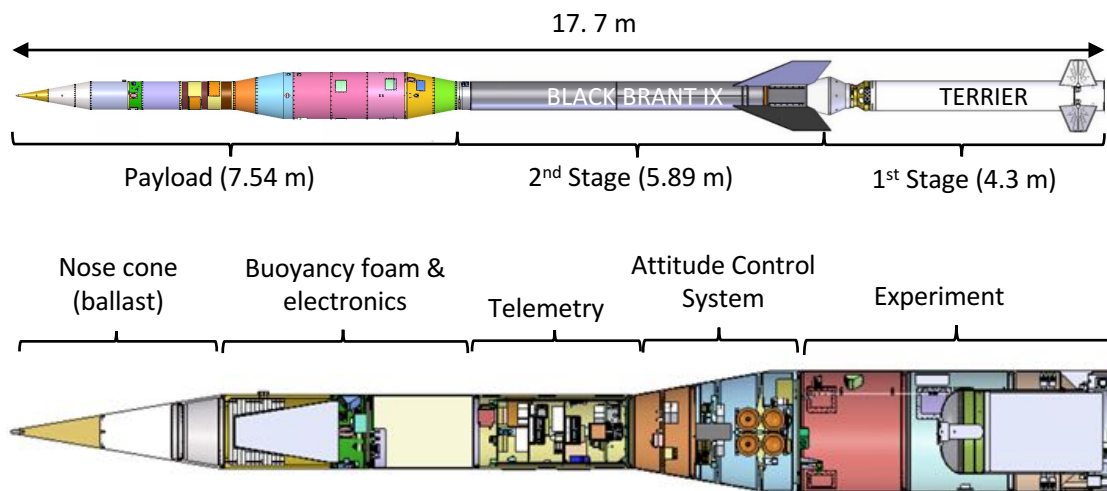
Mortar Fire
L+160-180 s
Alt: 38-40 km
$q_\infty$: 670-9300
Pa
Mach: 1.85-2.0

Payload Sep
~L+104 s
Alt: 48 to 35 km
Mach: 1.8

Line Stretch
MF+~1 s
$q_\infty$: 750-1030
Pa
Mach: 1.8 – 2.0

2nd stage Brant burnout
~L+34 s
Alt: ~16 km
Mach: 3.3 to 3.4

Peak Load
MF+~2 s
$q_\infty$: 750-1020 Pa
Mach: 1.75 to
2.0

2nd stage Brant Ignition
~L+8.0 s
Alt: ~1.5 km

Nosecone
Jettison
Alt: 3 km

1st stage Terrier burnout
~L+6 s
Alt: 0.9 to 1 km

Splashdown
L +~30 min

Atlantic Ocean

WFF Launch
Site

~60 -100 km

**Figure 1**.  **ASPIRE concept of operations.**



17. 7 m

BLACK BRANT IX

TERRIER

Payload (7.54 m)

2nd Stage (5.89 m)

1st Stage (4.3 m)

Nose cone
(ballast)

Buoyancy foam &
electronics

Telemetry

Attitude Control
System

Experiment

**Figure 2**.  **Schematic of the ASPIRE launch configuration and payload.**



Circumferentials

Radials

Suspension
lines

$d$

$L_R$

$L_B$

$L_S$
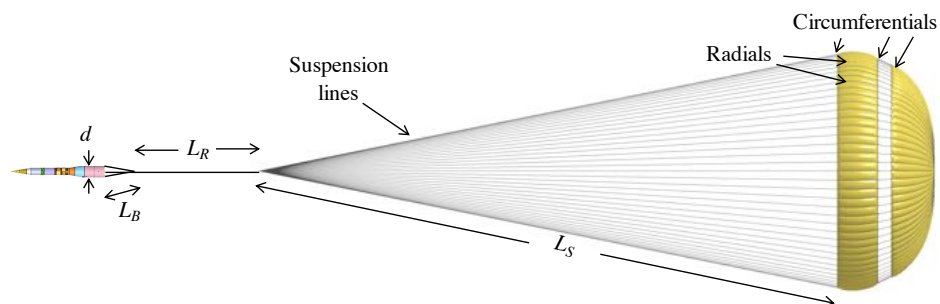
**Figure 3**.  **ASPIRE parachute system.**

3

**Table 2**. **Key Instrumentation Summary**

| Device | Sample Rate / Resolution | Notes |
|---|---|---|
| GLN-MAC IMU | 400 Hz | Provides both 100 Hz and 400 Hz raw data |
| Javad TR-G2 GPS | 20 Hz | |
| Load Pins | 1 kHz | 90 klbf rated, calibrated to 30 klbf (SR02) or 40 klbf (SR03) |
| HS Cameras (x3) | 1000 fps, 3840x2400 | Global shutter, 12-bit grayscale images |
| Situational Video (x2) | 120 fps, 1920x1080 | Rolling shutter |
| Situational Video (x1) | 30 fps, 3840x2160 | Rolling shutter |

a near-zero total angle of attack leading up to parachute deploy. Two pairs of roll-axis thrusters (a clockwise pair and a counter-clockwise pair) were used to zero-out any residual roll rate following de-spin and separation from the second stage.

The NIACS was also responsible for triggering the parachute deployment sequence at the desired dynamic pressure. During flight, the NIACS computed an onboard trajectory from the IMU measurements and GPS-derived position and velocity. This navigation solution provided an estimate of the inertial velocity and altitude throughout the flight. Prior to launch, polynomial models for atmospheric winds, density, and temperature as a function of altitude were loaded onto the NIACS. These polynomials were then evaluated during flight to obtain an onboard estimate of the wind-relative dynamic pressure which was used to trigger parachute deployment as described in Section 3.

*GPS receiver*—The ASPIRE payload contained a Javad TR-G2 HDA GPS unit that was repackaged into an mJAGR NSROC enclosure. A single wrap-around antenna was located at the aft end of the telemetry section. The GPS solution was provided to the NIACS and telemetered as a single serial stream. Data was provided at a 20 Hz solution rate.

*Triple bridle load pins*—To measure the loads imparted by the parachute, three load pins were installed on the instrumentation ring, which sits above the mortar tube. Each load pin interfaced with one leg of the parachute triple bridle, thus allowing for individual leg loads to be measured and a force vector to be calculated. The load pins were custom Strainsert units rated to a 90 klbf load capacity. Each load pin was paired with a Raetech miniature programmable strain gauge signal amplifier. On SR02, the signal amplifiers were equipped with a 240 Hz low-pass filter. To allow better resolution of snatch events associated with parachute deploy, a 50 kHz low-pas filter was used on SR03. Though rated for higher loads, the load pin and signal amplifiers were calibrated to a peak load of 30 klbf per pin on SR02, and a peak load of 40 klbf per pin on SR03. The calibration ranges were selected to reduce the uncertainty in the load pin measurements while ensuring that the signal amplifiers would not saturate in the event that a single bridle was slack at peak load.

*Cameras*— Two sets of cameras were used to record the parachute deployment and inflation event: a set of high-resolution, high-speed (HS) cameras and a set of situational awareness cameras. The HS camera system consisted of three IDT OS-10 cameras paired with a ruggedized Schneider APO-Xenoplan 2.0/20mm compact C-mount lens. The cameras recorded 12-bit grayscale images at 1000 frames per

second and a 4k resolution. Recording was performed with an aperture of 4.0 and a 40 $\mu$s exposure time.

The situational awareness cameras were a set of three standard GoPro Hero 4 cameras. The GoPros provided a wider angle contextual view and an NTSC feed that was telemetered during the flight. Two of these were set to record at 1080p and 120 fps and to telemeter video over NTSC during flight. The remaining GoPro was set to record 4K video at 30 fps.

*Range instrumentation*—Tracking of the sounding rocket and payload was provided via a C-band transponder and skin track from three ground-based radars. The radar data was provided at either 10 Hz or 50 Hz, depending on the radar.

## 3. MISSION OPERATIONS

*Launch and Powered Flight*

The SR02 launch window opened at 14:00 UTC (10:00 EDT) on the morning of March 31, 2018. Due to adverse weather conditions in the ocean recovery area, launch of the Terrier-Black Brant sounding rocket was delayed until 16:19 UTC (12:19 EDT). In contrast, launch of the SR03 sounding rocket was commanded at 13:30 UTC (09:30 EDT) on September 7, 2018, at the opening of the launch window. Figure 4 shows an overview of the payload trajectories during SR02 and SR03. Key events in the trajectories are indicated by the symbols. Tables 3 and 4 list key events and event conditions on SR02 and SR03, respectively.

Following ignition of the Terrier first stage, a set of six redundant lanyards were pulled on first motion of the payload on the launcher rails. This initiated a series of autonomous events on the test vehicle, all of which executed as planned. First, the computation of the NIACS navigation solution was initiated immediately following lanyard pull. Approximately a second later, a set of spin motors on the first stage fired to spin up the payload and boosters. The first stage burned out approximately 6 seconds after launch and separated from the second stage shortly thereafter.

The second stage motor was ignited approximately 8 seconds after launch and fired for 26 seconds. A yo-yo despin mechanism deployed approximately 100 seconds after launch. The residual spin rate was approximately 37 deg/s on SR02, and 48 deg/s on the heavier SR03 payload. Approximately 104 sec after launch, the payload separated from the second stage. On SR02, this occurred at an altitude of 53 km, which was significantly higher than the nominal prediction of 49.5 km. This over-performance was caused by an underprediction of the thrust provided by the second stage, and an overprediction of the drag on the payload and second stage. As a result, the thrust and drag models for the Black Brant MOD3 were updated prior to SR03. In SR03, payload separation occurred at an altitude of 48.1 km, approximately 1.5 km higher than the pre-flight nominal prediction.

*Experiment Phase*

The experiment phase of the flight began following separation of the payload from the second stage, at which time the ACS was enabled. Once the ACS was enabled, the payload angle of attack and sideslip decreased sharply and remained well below 5 deg until the start of the parachute phase in both flights, as shown in Figure 5. The roll rate was reduced to less than 0.6 deg/s by the action of the roll thrusters. Figure 6 shows the trajectories of the payload from second

**Table 3**. SR02 trajectory conditions at key test events.

| Event | Time from Launch sec | Mach | Dynamic Pressure Pa | Wind-Relative Velocity m/s | Geodetic Altitude km | Flight Path Angle deg |
|---|---|---|---|---|---|---|
| Launch | 0.0000 | 0.02 | 33.27 | 7.19 | −0.03 | 5.7 |
| Spin Up | 1.1880 | 0.21 | 3298.22 | 71.68 | 0.01 | 75.6 |
| Terrier Burnout | 6.2051 | 0.84 | 44 221.51 | 278.29 | 1.06 | 72.0 |
| Brant Ignition | 7.9581 | 0.78 | 36 103.35 | 256.95 | 1.50 | 71.6 |
| Mach 1.0 | 11.6981 | 1.00 | 52 522.03 | 330.64 | 2.54 | 71.5 |
| Mach 2.0 | 22.8454 | 2.00 | 109 113.38 | 617.98 | 7.45 | 71.2 |
| Mach 3.0 | 30.3065 | 3.00 | 110 459.42 | 888.61 | 12.70 | 68.9 |
| Brant Burnout | 34.0972 | 3.38 | 82 924.79 | 994.66 | 16.07 | 67.3 |
| Despin Begin | 100.0266 | 1.29 | 65.22 | 415.95 | 52.18 | 32.7 |
| Payload Separation | 103.9923 | 1.24 | 53.80 | 398.06 | 53.00 | 28.0 |
| Apogee | 123.4943 | 1.10 | 33.62 | 353.25 | 54.82 | 0.0 |
| NIACS Trigger | 176.0145 | 1.92 | 567.13 | 613.20 | 41.62 | −55.1 |
| Mortar Fire | 177.5879 | 1.97 | 670.63 | 626.75 | 40.77 | −55.8 |
| Line Stretch | 178.6255 | 2.00 | 744.57 | 636.42 | 40.27 | −56.2 |
| Peak Load | 179.0813 | 1.97 | 746.50 | 626.07 | 40.03 | −56.4 |
| 2nd Peak Load | 179.2733 | 1.89 | 694.69 | 600.03 | 39.93 | −56.4 |
| Mach 1.4 | 180.7190 | 1.40 | 416.55 | 444.26 | 39.31 | −56.9 |
| Mach 1.0 | 182.8645 | 1.00 | 233.10 | 316.05 | 38.63 | −59.4 |
| Mach 0.5 | 193.4312 | 0.50 | 76.88 | 154.75 | 36.63 | −75.9 |
| Nose Cone Jettison | 1568.4740 | 0.03 | 31.38 | 8.24 | 2.93 | −72.7 |
| Splashdown | 2029.5677 | 0.02 | 41.37 | 7.77 | 0.02 | −49.3 |

**Table 4**. SR03 trajectory conditions at key test events.

| Event | Time from Launch sec | Mach | Dynamic Pressure Pa | Wind-Relative Velocity m/s | Geodetic Altitude km | Flight Path Angle deg |
|---|---|---|---|---|---|---|
| Launch | 0.0000 | 0.03 | 59.42 | 10.00 | −0.041 | −4.97 |
| Spin Up | 1.1116 | 0.18 | 2317.96 | 62.54 | −0.007 | 69.66 |
| Terrier Burnout | 5.5466 | 0.82 | 44 160.69 | 283.71 | 0.845 | 74.56 |
| Brant Ignition | 8.0292 | 0.74 | 33 439.68 | 254.14 | 1.483 | 73.49 |
| Mach 1.0 | 12.2166 | 1.00 | 52 656.25 | 339.32 | 2.666 | 71.97 |
| Mach 2.0 | 23.6467 | 2.00 | 109 494.76 | 639.81 | 7.840 | 68.50 |
| Mach 3.0 | 30.6971 | 3.00 | 120 011.05 | 883.27 | 12.764 | 66.56 |
| Brant Burnout | 33.7250 | 3.29 | 94 687.38 | 946.14 | 15.334 | 66.15 |
| Despin Begin | 100.1504 | 1.21 | 111.61 | 387.02 | 47.560 | 23.95 |
| Payload Separation | 104.0617 | 1.17 | 96.41 | 372.53 | 48.101 | 18.69 |
| Apogee | 116.5281 | 1.11 | 79.36 | 354.82 | 48.846 | 0.00 |
| NIACS Trigger | 162.2427 | 1.81 | 808.57 | 563.14 | 38.821 | −51.10 |
| Mortar Fire | 163.8197 | 1.85 | 931.71 | 575.79 | 38.120 | −51.86 |
| Line Stretch | 164.8469 | 1.88 | 1028.44 | 584.67 | 37.645 | −52.54 |
| Peak Load | 165.2568 | 1.85 | 1020.12 | 573.21 | 37.455 | −52.77 |
| 2nd Peak Load | 165.4604 | 1.73 | 909.60 | 537.62 | 37.365 | −52.93 |
| Mach 1.4 | 166.1498 | 1.40 | 615.49 | 434.46 | 37.098 | −53.94 |
| Mach 1.0 | 167.5872 | 1.00 | 333.60 | 311.55 | 36.667 | −55.78 |
| Mach 0.5 | 174.6269 | 0.50 | 99.76 | 154.99 | 35.393 | −70.28 |
| Nose Cone Jettison | 1485.8200 | 0.03 | 48.50 | 10.53 | 3.155 | −78.91 |
| Splashdown | 1982.2182 | 0.02 | 34.99 | 7.78 | −0.004 | −69.78 |

stage separation until shortly after mortar fire. On SR02, the payload reached apogee at 54.8 km approximately 23 sec after separation. On SR03, the apogee altitude of 48.8 km was achieved 12 sec after separation. As the payload descended through the atmosphere, the Mach number and dynamic pressure increased as the payload accelerated. Parachute deployment was triggered by the NIACS during the descending portion of the trajectory.

The NIACS trigger initiated a series of events leading up to parachute deploy and inflation. Due to timing delays internal to the IDT cameras, these were not expected to capture images until a little over one second after the signal to begin recording was received. Therefore, the three science cameras were commanded to begin recording immediately after the NIACS trigger was activated, while a 1.4 sec delay between trigger and ignition of the gas generators in the parachute mortar was introduced by means of a pair of redundant timers.

The target parachute deployment conditions for SR02 and SR03 were selected to expose the strengthened parachutes to progressively larger aerodynamic loads. Only the dynamic pressure was used as a trigger condition and the ascent trajectory was designed so as to achieve a Mach number near 1.7 at the desired dynamic pressure. Models for the dynamics of the payload in the interval between trigger and parachute peak load and for the deployment and inflation of the parachute were used to determine the trigger parameters that would yield the desired dynamic pressure at peak load [18], [19]. These parameters were updated on the day before launch, using the latest meteorological forecasts for the time of launch. For SR02, it was determined that the NIACS should trigger when the onboard estimate of the dynamic pressure reached 532 Pa for a targeted dynamic pressure at full inflation of 678 Pa. On SR03, the target dynamic pressure for the NIACS trigger was 780 Pa and the estimated dynamic pressure at full inflation was 953 Pa.

On SR03, the dynamic pressure derived from the NIACS navigated solution reached the target value of 780 Pa 162.2 sec after launch. The dashed red line in Figures 5 and 6 indicate the instant at which the NIACS trigger was activated on SR03.
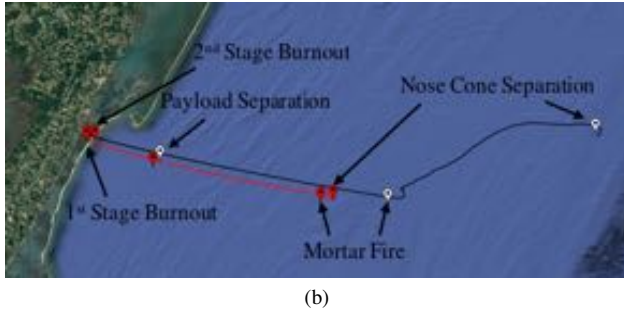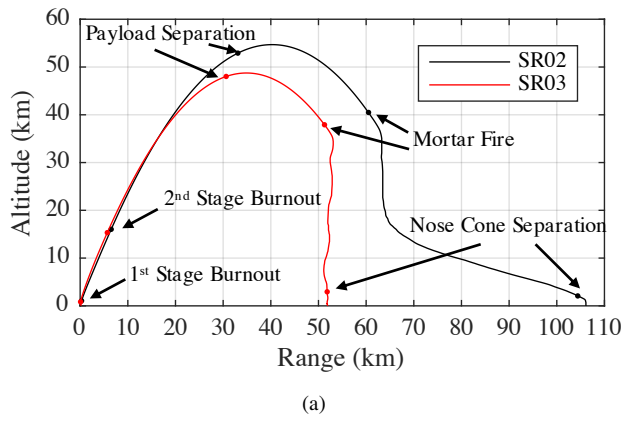
(a)



(b)

**Figure 4**. **Overview of the payload trajectory: a) Altitude vs. range; b) Ground track.**

From post-flight reconstruction, it was determined that the dynamic pressure at the time of NIACS trigger was 808.6 Pa and the Mach number was 1.81. At the time of mortar fire, approximately 1.5 sec later, the payload was at an altitude of 38.1 km above sea level. The wind-relative Mach number and dynamic pressure were approximately 1.85 and 932 Pa, respectively.

The target conditions for SR02 were defined assuming a launch between 8am EDT and 11am EDT. However, adverse weather conditions early in the morning of launch led to the launch window being shifted later in the day, and launch occurred at 12:19pm EDT. The changing weather conditions also resulted in significant differences between the atmospheric profiles uploaded to the NIACS and the atmosphere at the time of flight. As a result, the dynamic pressure at the time of NIACS trigger was 6.6% higher than the target value: 567.1 Pa. In addition, due to the overperformance of the second stage on SR02, the Mach number at trigger was also significantly higher than expected (1.92 vs. 1.72). At the time of mortar fire, the dynamic pressure had risen to 670.6 Pa and the Mach number was 1.97.

On both flights, the parachute deployed and inflated successfully and the vehicle decelerated rapidly, reaching subsonic speeds within approximately 6 sec of mortar fire. The payload then descended to the ocean while suspended beneath the parachute over a period of approximately 30 minutes. Throughout both flights, all numerical instrumentation on the payload performed as planned and collected the desired data. Real-time telemetry and situational awareness video from two of the GoPro cameras were relayed to the WFF range via S-band. Additionally, the payload was tracked throughout by up to three WFF radars.

On SR02 and SR03, all high speed cameras functioned properly and remained synchronized throughout the flight. The images from these cameras can therefore be used to conduct a stereographic reconstruction of the canopy shape during inflation.
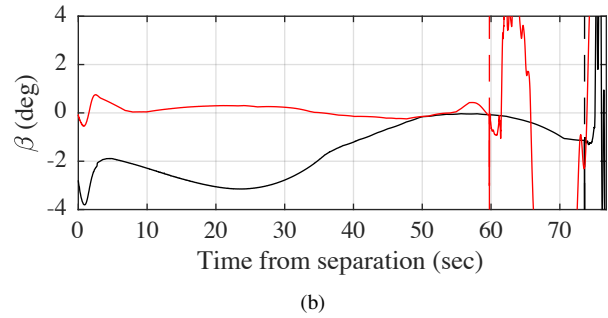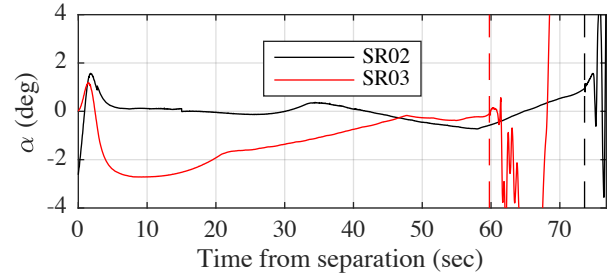


(a)



(b)



(c)
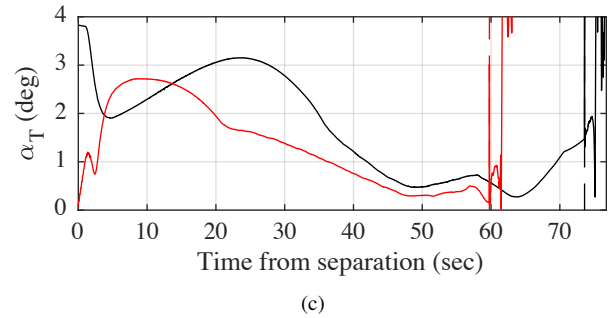
**Figure 5**. **Payload attitude from second stage separation until mortar fire. The dashed lines indicate the time at which the NIACS trigger condition was met on each flight.**

*Recovery*

Recovery operations for the payload and parachute began during the early morning of the day of launch. Splashdown predictions provided by the ASPIRE flight dynamics team were used to position two recovery vessels: a "fast-boat" designed to be the first on scene and the primary recovery vessel, the *Thomas Reed*. The purpose of the fast-boat was to attach flotation aids to the parachute upon arrival at the splashdown location to prevent the parachute and payload from from sinking prior to the arrival of the *Thomas Reed*. Spotter aircraft were also dispatched to provide visual tracking of the payload and parachute on descent and contact with the water.

On SR02, range safety considerations required that the recovery vessels be kept away from the predicted splashdown zone, and sea conditions limited the speed that both boats
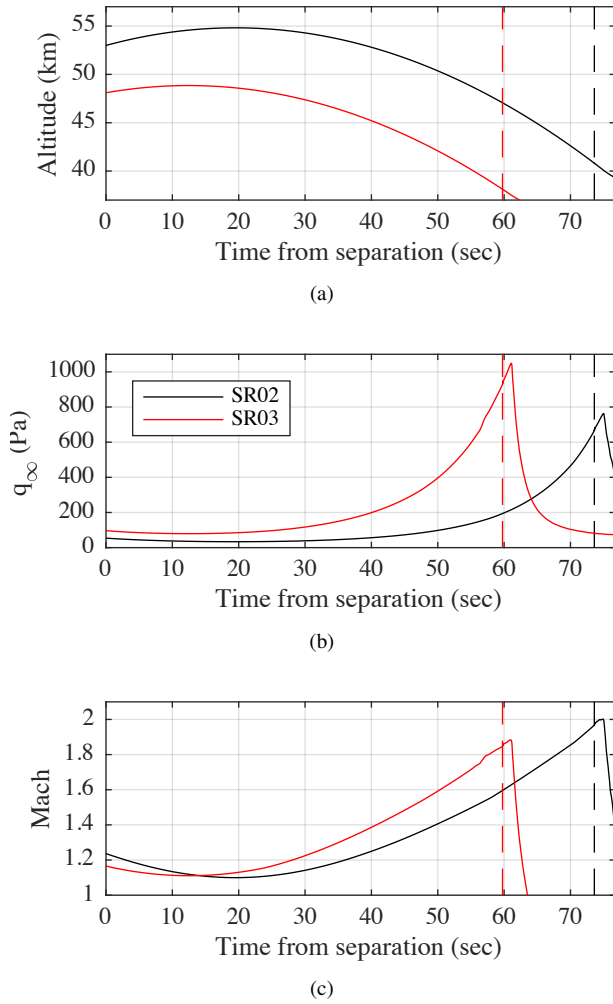
(a)



(b)



(c)

**Figure 6**. **Payload trajectory from second stage separation until mortar fire. The dashed lines indicate the time at which the NIACS trigger condition was met on each flight.**

could travel. As a result, the recovery vessels did not arrive at the payload until 45 minutes after splashdown, after the parachute had become completely submerged. Due to sea state conditions, recovery operations were considerable more challenging than during SR01 [17], but both payload and parachute were recovered without significant damage.

In contrast, the SR03 recovery proceeded smoothly and the team did not need to rely on many of the precautions put in place prior to launch. The splashdown predictions provided on the day before launch were found to be within a quarter of a nautical mile of the actual splashdown location. As a result, the recovery vessels were positioned within visual range of the payload during much of its descent. The parachute and payload were spotted by the recovery vessels shortly after parachute deployment, allowing for easy visual tracking from the deck of the vessels. The recovery vessels kept a safe distance from the payload until the ballasted nose cone was released at an altitude of 3 km, and then proceeded towards the splashdown location. An image of the payload captured from the deck of the *Thomas Reed* is shown in Figure 7.

Once retrieved from the ocean, the payload and parachute

were returned to shore. The items were rinsed down to remove salt deposits and the parachute was hung to dry over several days.



**Figure 7**. **SR03 payload during descent, as seen from the recovery vessel.**

## 4. ATMOSPHERE AND TEST CONDITIONS

Knowledge of the atmospheric state at the altitudes of interest (from the surface to approximately 55 km) was achieved by combining in-situ measurements obtained using meteorological balloons carrying radiosonde payloads with atmospheric states obtained from NASA's Goddard Earth Observing System model version 5 (GEOS-5) [20].

On the day of launch, between 5 and 6 Totex TX-3000 high-altitude latex balloons were released at regular intervals starting 3 hours before launch. Each balloon carried a Lockheed Martin Sippican LMS-6 radiosonde to altitudes of between 35 km and 40 km. The LMS-6 radiosondes are equipped with a chip thermistor to measure atmospheric temperature as well as a differential GPS receiver for determining the sonde's position and velocity. The atmospheric winds as a function of altitude are determined from the horizontal velocity of the radiosondes throughout their ascent. The atmospheric density is determined from the measured temperature and altitude by assuming the air behaves as an ideal gas and that the atmosphere is in perfect hydrostatic equilibrium. No in-situ measurements were available above 40 km. Therefore, the atmospheric profile above this altitude was obtained from the GEOS-5 analysis for 15:00 UTC (11am local time) at Wallops Island.

Figures 8 through 11 show the reconstructed atmospheric profiles for the SR02 and SR03 launches. The solid lines denote the mean values, while the dashed lines indicated the corresponding $3\sigma$ bounds. Note that the wind speeds were near zero on SR03, as is typical for a late summer day at WFF. Similarly, the sustained westerly winds in the SR02 profile

are typical for March. However, the wind shear layer at approximately 10 km was significantly larger than is typical for the season. The difference in the splashdown locations seen in Figure 4 is largely due to these differences in the wind profiles.
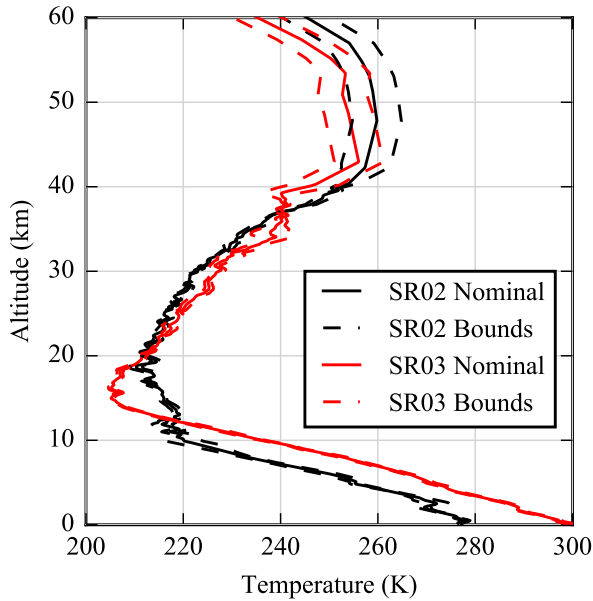


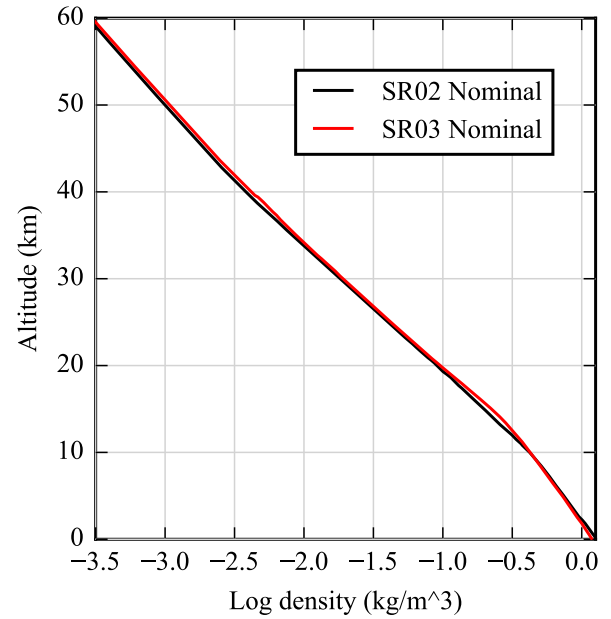**Figure 8**. **Reconstructed temperature profile for SR02 and SR03.**



**Figure 9**. **Reconstructed density profile for SR02 and SR03. The uncertainty bounds were omitted in this figure to reduce clutter.**

## 5. TEST ARTICLE PERFORMANCE

*Deployment*

In this paper, parachute deployment is defined as the events taking place between mortar fire and line stretch. Mortar fire began with two NASA Standard Initiators igniting the mortar's gas generator. Based on ground test data, the pack begins to move about 8 ms later and a series of Kevlar lanyards used to restrain the pack are broken. Imagery during the emergence of the pack was limited by the field of view of the HS cameras and by the sabot and sabot capture net blocking the camera view. However, the first signs of debris associated with mortar deployment appeared in the high speed cameras around 20 ms after mortar fire. This observation, along with ground test data, suggest that the pack was likely out of the mortar tube within 40 ms of mortar fire.

High speed imagery of the deployment event provided excellent views of the parachute pack as it emerged from the mortar tube and progressed to line stretch. Sequences showing the deployment of the parachute riser and suspension lines on SR02 and SR03 are provided in Figure 12 and Figure 13. Overall, the deployment was observed to be orderly with no entanglement on both flights. Some minor twisting and untwisting motion of the riser was visible as the suspension lines began to be deployed. The unfurling of the riser and lines also initiated small transverse waves throughout the deployment process. No major line sail was observed during the deployment on either flight.

In both flights, the parachute pack did not maintain a vertical orientation throughout the deployment process, but rather exhibited pitching and yawing motion. This behavior had been
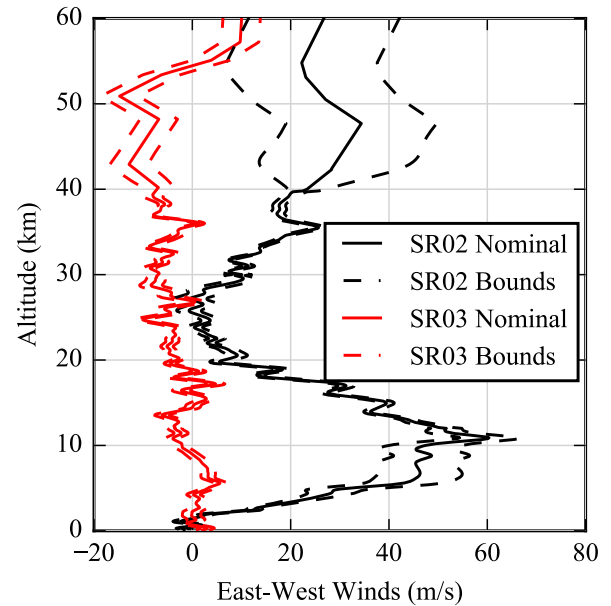


**Figure 10**. **Reconstructed East-West wind profile for SR02 and SR03.**
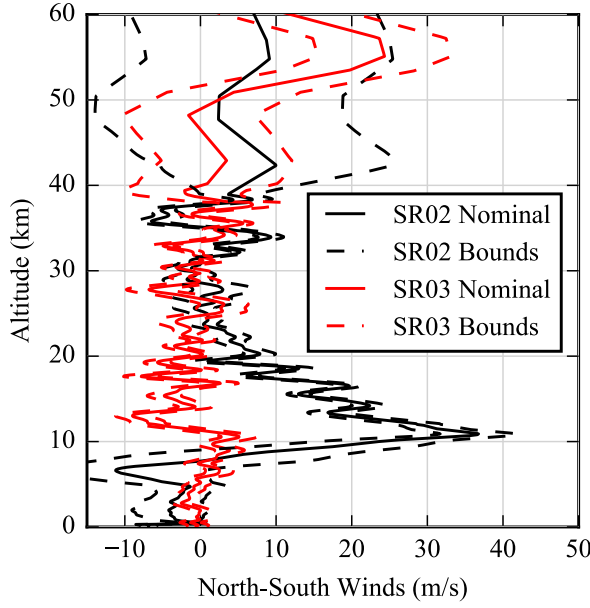
**Figure 11**. **Reconstructed North-South wind profile for SR02 and SR03.**

observed in previous deployments of supersonic parachutes from the PEPP, SPED, SHAPE, and BLDT test series [6], [7], [8], but was not present in SR01 [17]. However, the degree of rotation observed on SR02 was larger than observed in prior supersonic tests.

Using as-built dimensions of the parachutes and the observed times from mortar fire to line stretch, the mortar velocity ($V_m$) was estimated as:

$$V_m = \frac{l_{ls} + 0.5 a_v t_{ls}^2}{t_{ls}} \qquad (1)$$

where $l_{ls}$ is the distance to line stretch, $t_{ls}$ is the time to line stretch, and $a_v$ is the average deceleration of the payload during the deployment sequence. Note that this estimate neglects bag drag or friction from the lines emerging from the bag. Using average measurement values for the lengths of the suspension lines, bridles, and riser along with the dimensions of the confluence fitting, the distance to line stretch was calculated as 45.59 m. Figures 16 and 17 show the time history of the measured tension on the three triple bridles during the deployment and inflation process. In Figure 16, a rise in tension associated with line stretch is visible starting approximately 1.038 sec after mortar fire. In Figure 17, a similar rise is evident 1.027 sec after mortar fire. The time to line stretch was defined as the time from parachute pack ejection to the *beginning* of the increase in line tension. This yielded an estimate of $t_{ls} = 0.998$ sec on SR02, and $t_{ls} = 0.987$ sec on SR03. The pack velocity at the exit plane of the mortar was thus calculated as 46.7 m/sec on SR02 and 47.3 m/s on SR03. However, the mortar reaction load also applied a small increase in velocity of approximately 3.5 m/s to the payload. When accounting for this increment, the pack velocity compares well with the velocities measured during mortar ground testing (approximately 44 m/sec).

In Figures 16 and 17, a large spike in tension is evident approximately one second prior to line stretch. This peak is associated with two near-simultaneous snatch events: the arresting of the 5.2 kg mortar sabot by a capture net integrated into the triple bridle and the arresting of the 3.7 kg titanium confluence fitting linking the parachute riser to the triple bridle. On SR03, the 240 Hz low-pass filter on the signal amplifiers was replaced with a 50 kHz filter to better capture these snatch events.

*Inflation*

Inflation is defined here as beginning at the moment of line stretch, when the leading edge of the canopy first emerges out of the parachute pack. Sequences showing the progression of canopy inflation on SR02 and SR03 are provided in Figures 14 and 15 . In both flights, portions of the canopy are visible beginning less than 100 ms after line stretch and by 200 ms after line stretch a portion of the band can be seen to be inflating outwards. Video imagery of the inflation sequences showed that this portion of the band led the inflation process briefly but then began to stall. Once the band had opened enough, air progressed further back towards the disk and began pressurizing the portion of the disk near the region of the band leading the inflation. From that point forward, the inflation appeared largely symmetric. The vent remained nearly circular throughout, indicating a relatively symmetric distribution of radial loading.

The time at full inflation is defined as the instant when the parachute first achieved peak load. On SR02, this occurred 1.493 sec after mortar fire, as seen on Figure 16. On SR03, this occurred 1.437 sec after mortar fire. This yielded a time from line stretch to full inflation of 0.456 sec for SR02, and 0.410 sec for SR03. For comparison, the MSL build-to-print parachute was found to inflate in 0.635 sec at Mars and in 0.506 sec on Earth during SR01. Prior to flight, the inflation time was modeled following the approach proposed by Greene [21]. The time necessary to achieve full inflation was based on a required inflation distance $l_{inf}$ needed to ingest the volume of gas necessary to fully inflate the canopy. The inflation distance was modeled as:

$$\frac{l_{inf}}{D_0} = \alpha_{inf} \left( \frac{\rho_c}{\rho_\infty} \right) \qquad (2)$$

where $\alpha_{inf}$ is a non-dimensional canopy-specific parameter related to the parachute's volume, nominal diameter, and effective inlet area during inflation. For supersonic inflations, a normal shock is assumed to develop ahead of the canopy inlet, and the ratio of the density inside the canopy to the freestream density ($\rho_c/\rho_\infty$) is given by the ratio of the stagnation density behind the shock to the freestream static density. For the sounding rocket tests, this ratio was computed assuming inflation in dry air and using the Mach number at line stretch listed in Tables 3 and 4. The inflation distance was calculated by integrating the payload velocity from line stretch to the instant when peak load was achieved. This yielded a value of $\alpha_{inf} = 4.29$ for SR02 and $\alpha_{inf} = 3.75$ for SR03, which is in decent agreement with ASPIRE SR01 ($\alpha_{inf} = 4.77$) and with recent supersonic parachute inflations from the Phoenix ($\alpha_{inf} = 4.8$), MSL ($\alpha_{inf} = 4.6$), and LDSD projects ($\alpha_{inf} = 5.2$ and 4.5).

In addition to the individual load pin measurements, Figures 16 and 17, show the total tension during deployment and inflation. The peak tension at full inflation was 47.7 klbf on SR02 and 63.2 klbf on SR03. However, because of the deceleration on both the payload and the parachute, the total parachute force generated is comprised of both the tension in the bridles and the contribution from the deceleration of the parachute system. Using the time history of the deceleration
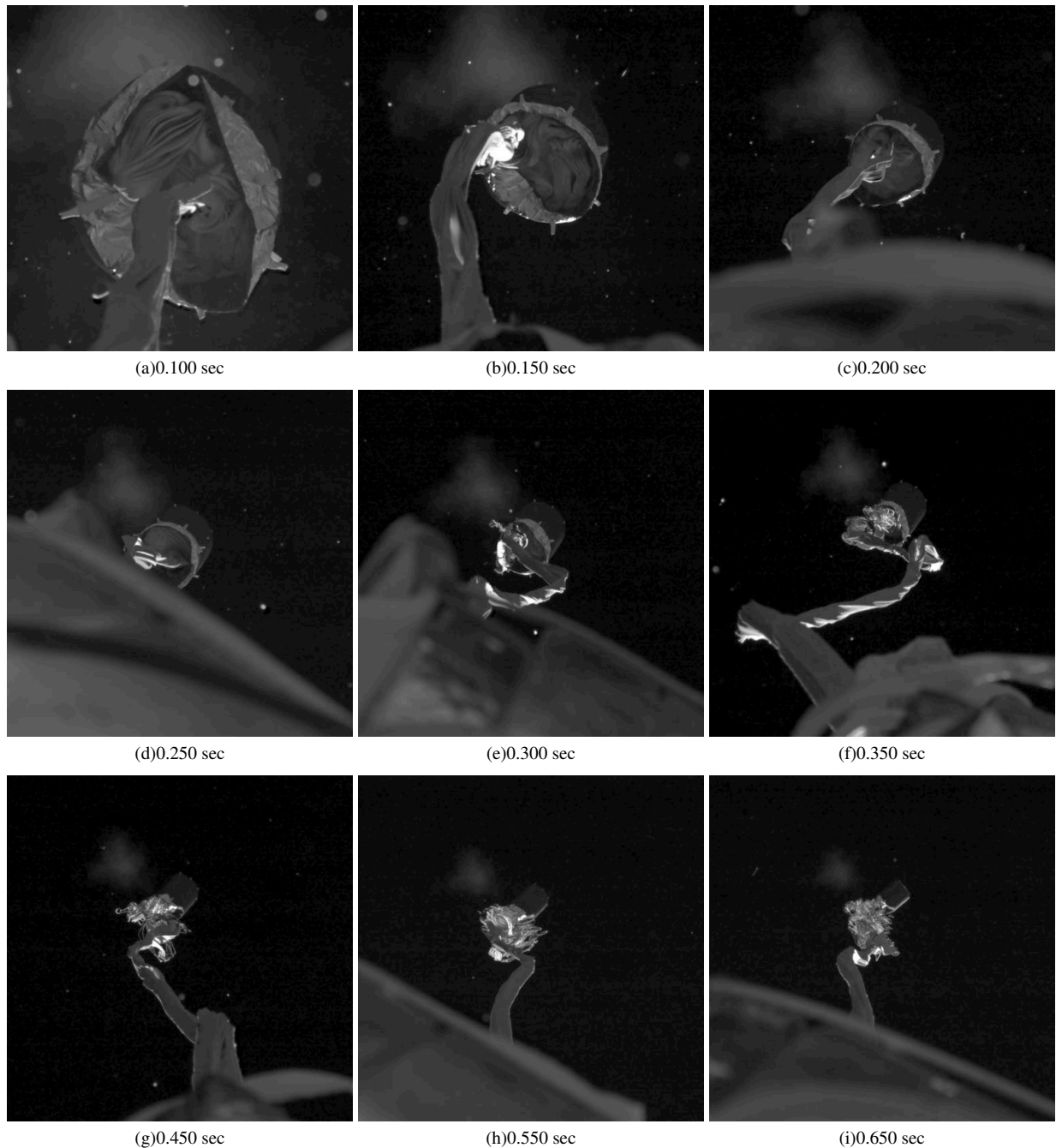
9

|  |  |  |
|---|---|---|
| (a)0.100 sec | (b)0.150 sec | (c)0.200 sec |
| (d)0.250 sec | (e)0.300 sec | (f)0.350 sec |
| (g)0.450 sec | (h)0.550 sec | (i)0.650 sec |

**Figure 12**. **SR02 parachute deployment sequence. Times are relative to mortar fire.**

during inflation, the peak load at full inflation was found to be 50.9 klbf for SR02 and 67.4 klbf for SR03.

After peak load, a large decrease of over 50% of the load occurred over about 100 ms in both flights. From comparison with the HS imagery, this load dip was found to roughly correspond to a partial rebound in the disk and band. In SR03, the tension then increased to 62.0 klbf (total parachute force was 66.5 klbf). On SR02, the tension increased to a second peak that was higher than the first peak force: 52.6 klbf. This resulted in a total parachute force of 55.8 klbf. On SR03, the canopy was observed to be mostly stable and free of large oscillations in area after the second peak in parachute load. On SR02, however, there was one additional drop in the

parachute area approximately 2.1 sec after mortar fire. Note also that on SR03 the load was distributed very evenly among the three bridles throughout inflation. On SR02, however, the load alternated between being biased towards LP1, and being biased on LP2 and LP3.

The last key observation from the inflation process entails the parachute bag. Since Viking, the parachute bag has been retained in all Mars parachutes to prevent recontact and potential damage to the canopy, as was often seen during PEPP flights. Generally this has been achieved through cords attached to the canopy at or near the vent. For the strengthened parachute, the bag was attached to the vent by means of lanyards sets (four sets in SR02, eight in SR03).

(a)0.100 sec     (b)0.150 sec     (c)0.200 sec

(d)0.300 sec     (e)0.400 sec     (f)0.500 sec

(g)0.600 sec     (h)0.800 sec     (i)1.027 sec
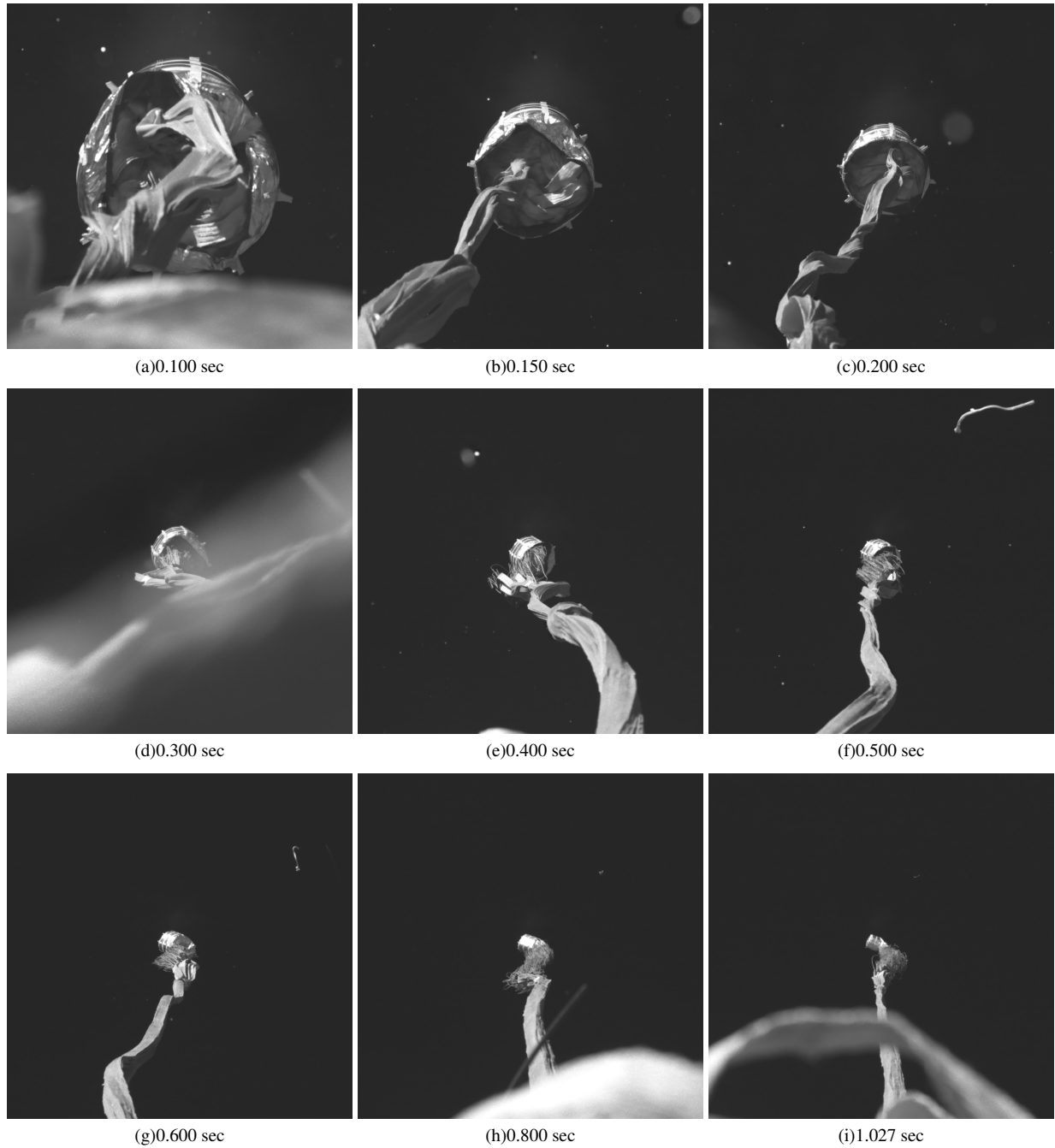
**Figure 13**. **SR03 parachute deployment sequence. Times are relative to mortar fire.**

Both the HS and situational awareness cameras showed that the bag was retained throughout the inflation process in both flights.

*Aerodynamic Performance*

The force exerted by the parachute on the payload was calculated by two independent methods: from the triple bridle load pin measurements and from the NIACS accelerometer data. The parachute drag force ($F_D$) was calculated by projecting the parachute force vector onto the wind-relative anti-velocity vector, and a parachute drag coefficient was computed as:

$$C_D = \frac{F_D}{q_\infty S_0} \quad (3)$$

where $q_\infty$ is the freestream dynamic pressure, and $S_0$ is the parachute reference area. The resulting time histories of $C_D$ during the first 30 sec following mortar fire are shown in Figure 18. A 50 Hz low-pass filter was applied to the SR03 results. Starting at line-stretch, $C_D$ increased rapidly and reached an initial peak value of approximately 0.81 in both SR02 and SR03. Immediately following this peak, $C_D$ decreased sharply to about 0.45 on both flights. Subsequently, $C_D$ peaked at a value of approximately 0.98 on SR02 and 0.88 on SR03. Following this second peak, on both SR02 and SR03, the value of $C_D$ remained between approximately 0.66 and 0.81 until the parachute entered the subsonic regime. Shortly after the parachute enter the subsonic regime, the $C_D$ decreased continuously for a period of 2 sec. After,

11

(a)0.000 sec

(b)0.100 sec

(c)0.200 sec

(d)0.300 sec

(e)0.400 sec

(f)0.500 sec

(g)0.600 sec

(h)0.700 sec

(i)0.800 sec
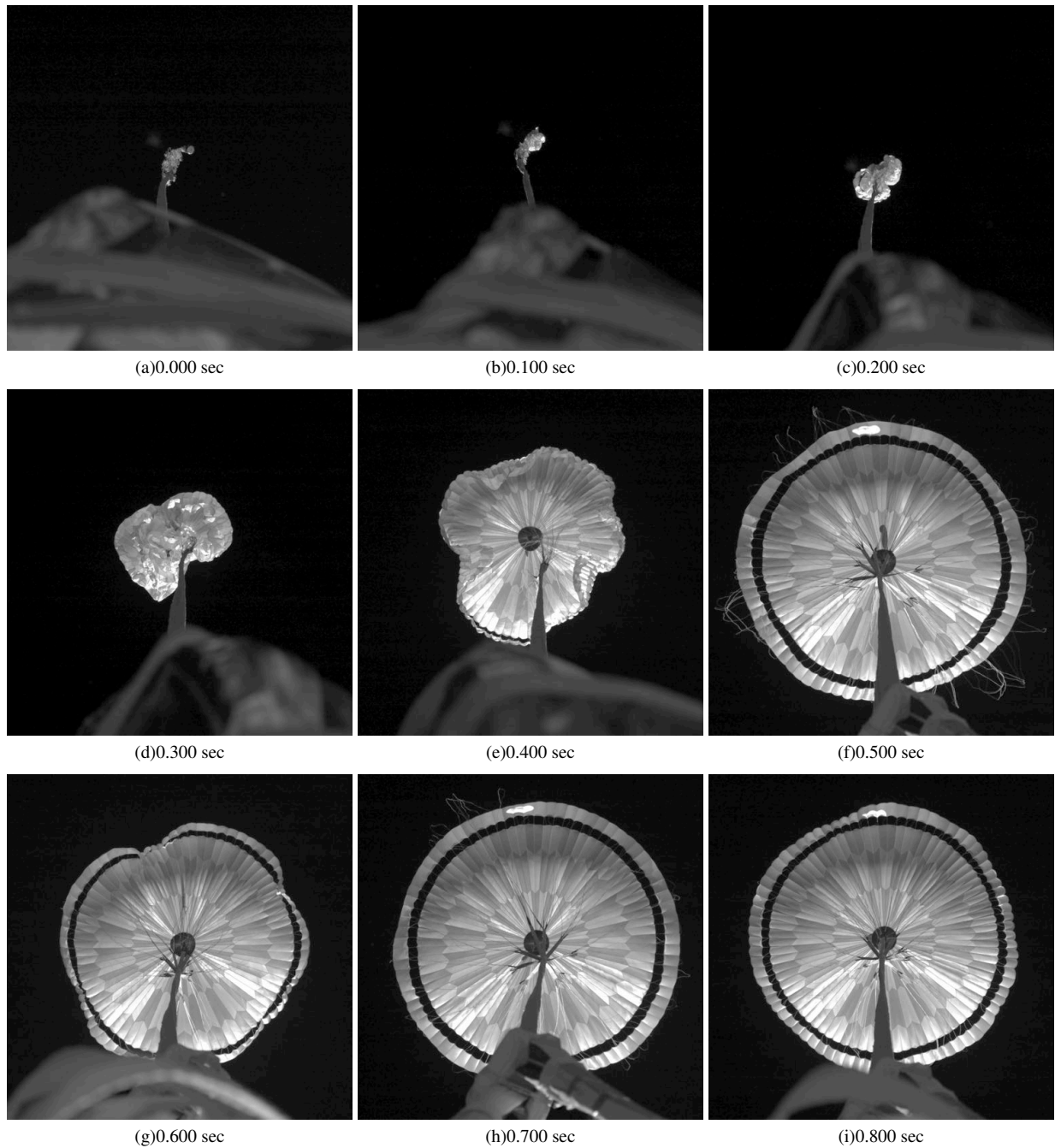
**Figure 14**. **SR02 parachute inflation sequence. Times shown are relative to line stretch.**

the decrease in the drag coefficient stopped, $C_D$ remained between 0.57 and 0.67.

The load pin and accelerometer results were in good qualitative agreement, and both values agreed within three standard deviations. However, note that the load pins were sized to record the peak inflation load. As such, they were capable of withstanding loads of up to 90 klbf and the uncertainty in their measurement of the total force was approximately 3% at peak load. During steady descent, however, the uncertainties in the load pin measurements reached 30% of the measured load. In contrast, the uncertainties in the forces determined from the measured accelerations remain well below 5% throughout. Thus, the results obtained using the acceleration measure-

ments were used to evaluate the performance of the parachute following full inflation.

Figure 19 shows the pre-flight model for the parachute drag coefficient, which was a function of the Mach number only. The solid blue line indicates the nominal values of $C_D$ as a function of Mach number in the preflight model, while the dashed blue lines indicate the pre-flight upper and lower bounds on $C_D$. The solid back and red lines denote the rolling average of the reconstructed $C_D$ from the NIACS measurements as a function of Mach number for SR02 and SR03, respectively. The averaging was performed over all values of $C_D$ in sliding bins of width Mach = 0.03. The results from the two flights are in excellent agreement with
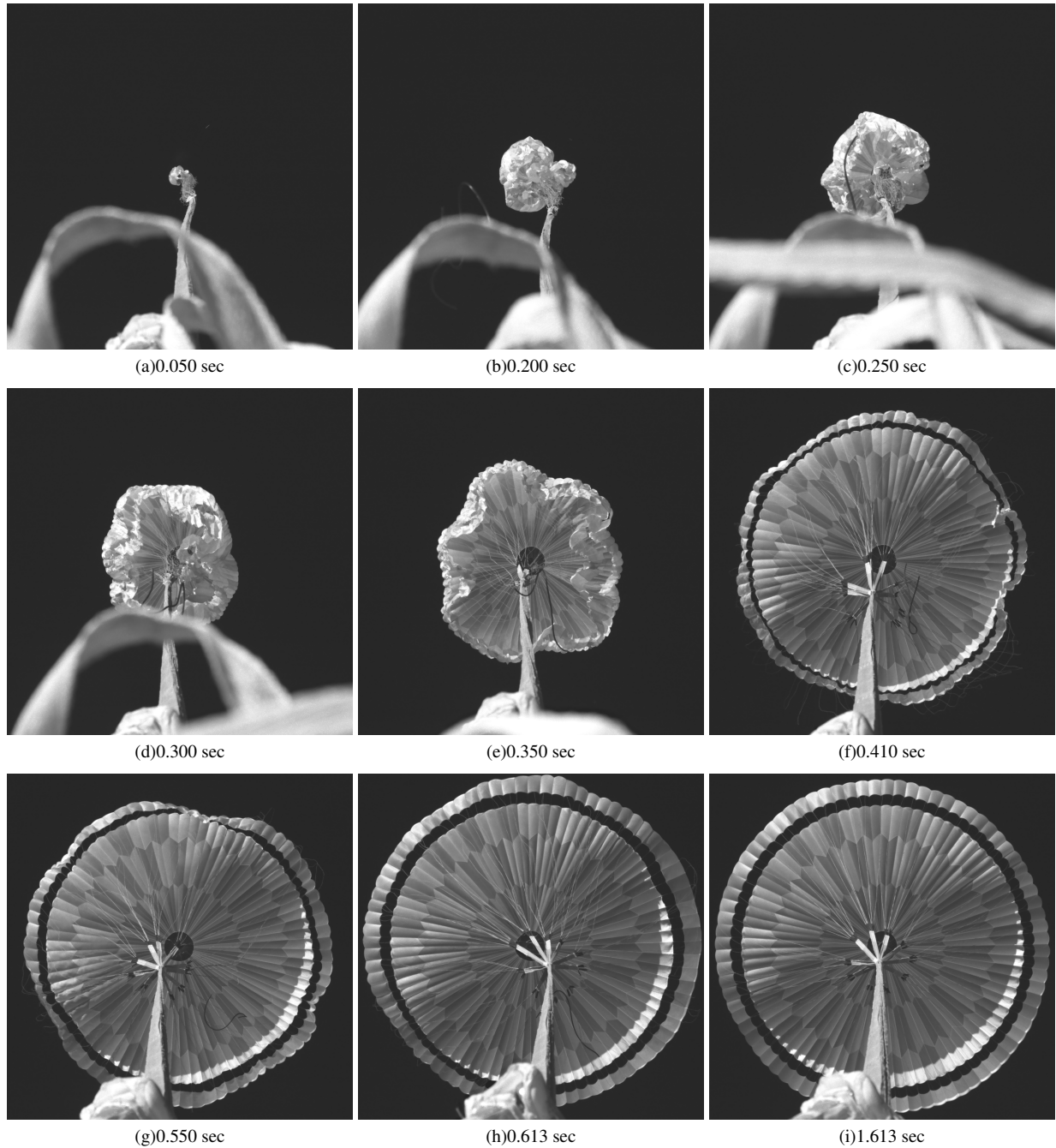
**Figure 15**. **SR03 parachute inflation sequence. Times shown are relative to line stretch.**

each other. At subsonic speeds, the observed parachute drag coefficient in SR02 and SR03 was in good agreement with the pre-flight model. The average reconstructed $C_D$ for Mach numbers below 0.75 was 0.626 for SR02 and 0.618 for SR03, which is in excellent agreement with the pre-flight nominal value for the drag coefficient in this Mach number range of 0.628. At Mach numbers above 1.1, however, the reconstructed $C_D$ was generally lower than the nominal pre-flight estimate. The reason for this discrepancy is currently being investigated and potential contributing factors have been identified. For example, the pre-flight model relied on assumptions about the dynamics of the parachute payload system as well as CFD simulations of an inflated canopy in the wake of the payload which are sensitive to the choice of

inflated geometry and location of the canopy within the wake. The stereoscopic reconstruction of the canopy shape will aid in improving these models for subsequent supersonic flights [22].

Figure 20 shows the time history of the dynamic pressure from mortar fire until 20 seconds after mortar fire. Following inflation, the dynamic pressure decreased rapidly. By the time the parachute entered the supersonic regime, the dynamic pressure on both flights had fallen to roughly 30% of the dynamic pressure at mortar fire.

Figure 21 shows the parachute pull angle: the angle between the parachute force vector and the vehicle centerline for SR02
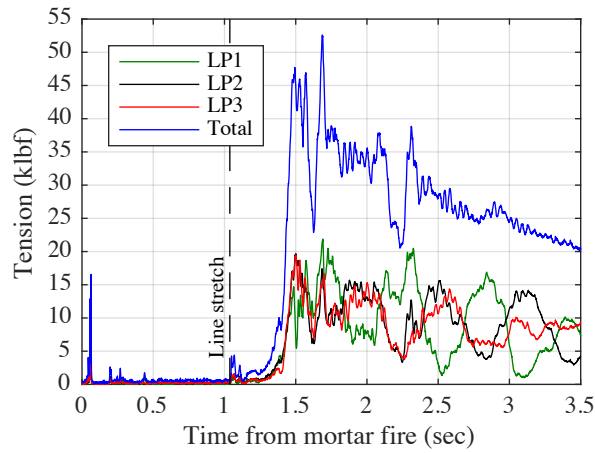
**Figure 16**. **Tension on the triple bridle legs and total load from from 0 to 3.5 sec after mortar fire, for SR02.**
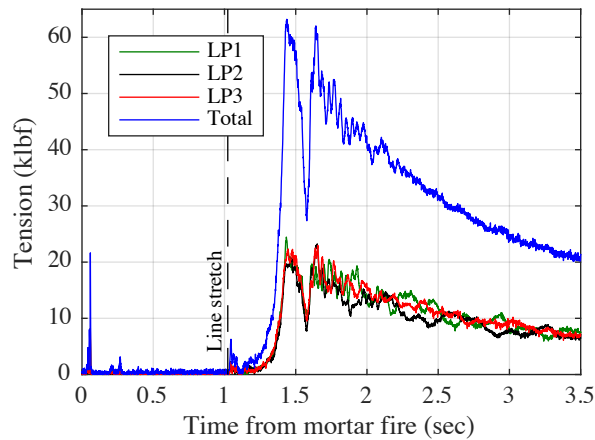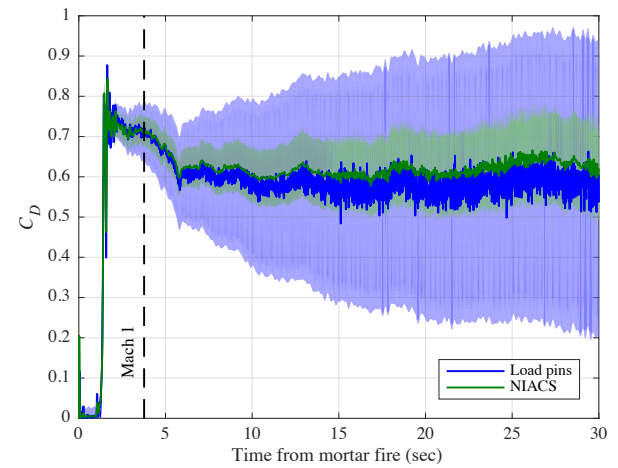


**Figure 17**. **Tension on the triple bridle legs and total load from from 0 to 3.5 sec after mortar fire, for SR03.**



(a)



(b)

**Figure 18**. **Reconstructed parachute drag coefficient during the first 30 seconds after mortar fire, using the NIACS and load pin measurements for: (a) SR02 (b) SR03. The shaded regions indicate the 3-$\sigma$ confidence interval.**

and SR03. Figure 21(a) shows the pull angle from line stretch until 5 sec after mortar fire, while Figure 21(b) shows the same quantity from 5 sec to 20 sec after mortar fire. On SR03, the pull angle remained below 2 deg once the inflation transients had settled. On SR02, however, the pull angle oscillated between 0 and 7 deg throughout. These oscillations are a results of the parachute imparting more significant dynamics to the payload on SR02.

The vehicle rotation rates during the early stages of the parachute phase are shown in Figure 22. Prior to mortar fire, the payload angular rates were very small on both flights owing to control by the NIACS. Although the ACS was disabled just prior to mortar fire, the rates remained small through mortar fire and line-stretch. Starting at line stretch on both flights, torques imposed by the tension on the bridles caused the payload to start oscillating in the pitch and yaw axes. On SR03, these rates remained below 30 deg/s for the first 5 seconds after mortar fire. On SR02, however, the torques imposed by the parachute on the payload were significantly larger due to the asymmetric distribution of loads on the bridles (Figure 16).

In particular, due to the small inertia of the payload about its roll axis (less than 50 kg-m$^2$), a large roll torque was imparted on the payload during inflation on SR02. Approximately 100 ms after full inflation, the roll rate increased from 0 to 40 deg/s, and remained roughly constant until approximately 1 sec later, when it increased to 180 deg/s. Figure 16 shows the time history of the tension in the three bridles from 0 to 3.5 sec after mortar fire on SR02. At full inflation, the tension measured by load pins LP2 and LP3 exceeded the tension on the remaining leg. This asymmetry in loading induced a positive torque about the roll axis of the payload, leading to the increase in roll rate to 40 deg/s. Approximately 1 sec after later, the roll rate increased again when the tension on LP1 exceeded that on the remaining two legs. A pattern of alternating asymmetrical loading followed, which resulted in the roll rate increasing to 180 deg/s. Throughout this process, the payload spun about its roll axis independent of the parachute, resulting in twisting of the riser line. The riser thus acted as a torsional spring which opposed the spinning of the payload. Starting 10 sec after mortar fire, this led to
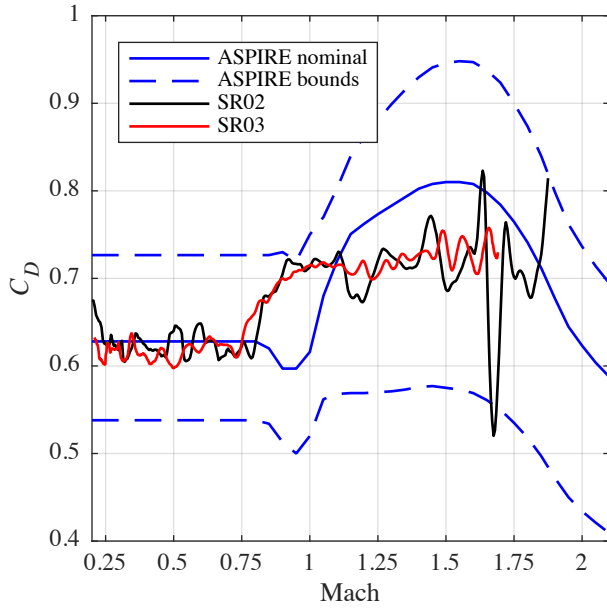
**Figure 19**. **Reconstructed $C_D$ coefficient as a function of Mach number from 1.68 sec. after mortar fire until subsonic terminal descent.**
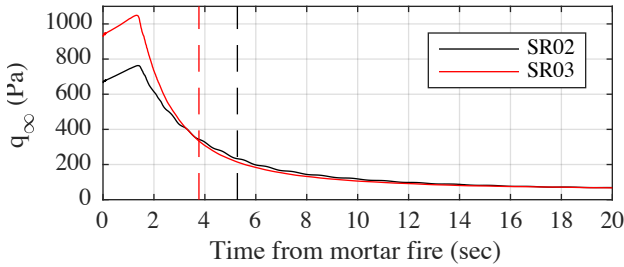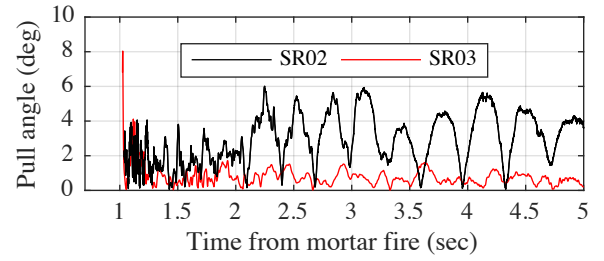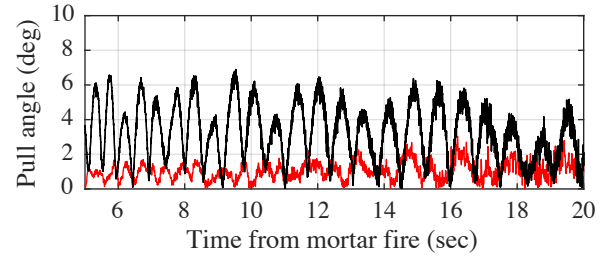


**Figure 20**. **Freestream dynamic pressure during the 40 seconds following mortar fire. The dashed lines indicate the times when the Mach number fell below 1.0 for each flight.**



(a)



(b)

**Figure 21**. **Reconstructed parachute pull angle (a) from line stretch to 5 seconds after mortar fire (b) from 5 to 20 seconds after mortar fire, from the load pin readings.**

a decrease in the roll rate and finally a reversal of the roll direction. As the payload began to spin in the negative roll direction, it once again twisted the riser, which acted as a torsional spring opposing the motion of the payload in the new direction. This process continued throughout the entire descent, and the payload was found to spin in alternating directions throughout the flight, as shown in Figure 23. Note that a disturbance to the system at an altitude of approximately 28 km temporarily disrupted the rolling motion, which resumed below 23 km.

On SR03, the payload roll rates remained below 30 deg/s throughout inflation and the initial phases of parachute flight. At an altitude of approximately 27 km, an external disturbance caused an increase in the parachute pull angle that imparted pitching and yawing torques on the payload. The pitching and yawing motion of the payload in turn resulted in alternating asymmetrical loading of the bridles, which induced a roll torque on the payload. Like in SR02, this resulted in twisting of the riser which acted as a torsional spring during the remainder of the descent.

Time histories of the payload wind-relative angle of attack and sideslip from line stretch until 20 seconds after mortar fire are shown in the first two panels in Figure 24. The third panel in Figure 24 shows the total angle of attack of the payload. In both flights, the total angle of attack began increasing immediately after full inflation. The increase in the total angle of attack continued until 6 to 8 sec after mortar fire, when it achieved a mean value of about 15 deg and continued to oscillate about this value. Throughout this period, $\alpha$ and $\beta$ oscillated owing to the rotation of the payload about its rolls axis.

*Post-Flight Inspection*

Once the parachutes were returned to shore after each flight, they were rinsed free of salt water and hung to dry before being shipped to US Naval Weapons Center China Lake for inspection. Post-flight inspection of the SR02 parachute revealed minimal damage. The majority of this damage appeared to be deployment-related and caused by interaction of the canopy with the bag or by friction between adjacent surfaces on the canopy. For example, Figure 25 shows the damage to the vent band at one of the four deployment bag attachment locations. To reduce the risk of damage to the SR03 canopy, the number of bag attachment locations was increased from four to eight, the mass of the deployment bag was reduced, the Technora bag attachment cords were replaced with more compliant Nylon cords, and the length of the energy modulators on the deployment bag was reduced. Post-flight inspection of the SR03 canopy that included these changes revealed almost no damage.

## 6. CONCLUSIONS AND FUTURE WORK

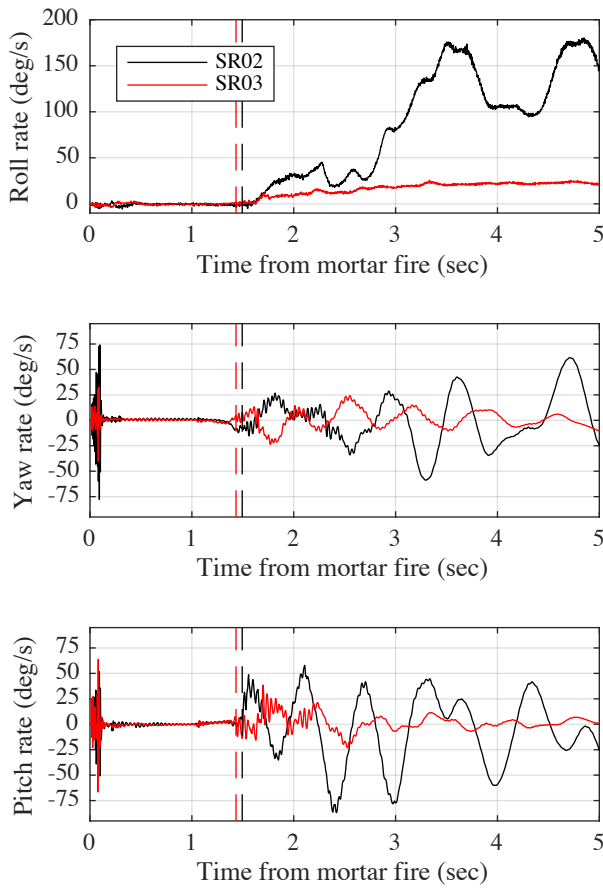The ASPIRE project's first two supersonic tests of a strengthened DGB (SR02 and SR03), took place on March 31 and

**Figure 22**. **Reconstructed vehicle rotation rates during the first 5 sec after mortar fire. The dashed lines indicate the time at which peak load was achieved.**



**Figure 23**. **Payload roll rate as a function of altitude during the parachute descent phase.**

September 7, 2018 at Wallops Island. The 21.45 m test articles were delivered to peak altitudes of 54.8 km and 48.8 km by a two stage sounding rocket platform. The parachute deployment sequence was triggered during the descending portion of the flight, when the payload achieved the target dynamic pressure as determined by the onboard navigation system. On SR02, the parachute was mortar-deployed at a Mach number of 1.97 and a dynamic pressure of 670 Pa, and produced a peak load of 55.8 klbf. During the SR03 flight, the parachute mortar was ignited at a Mach number of 1.85 and a dynamic pressure of 932 Pa, and the parachute produced a peak force of 67.4 klbf.

In both tests, the parachute deployment process proceeded in an orderly fashion. The parachute pack reached line stretch 1.038 sec after mortar fire on SR02 and 1.027 sec after mortar fire on SR03. The inflation of the parachutes also proceeded as expected, with no significant asymmetries or anomalies. Using Greene's non-dimensional inflation distance method [21], the inflation was found to be in family with recent supersonic parachute inflations from the Phoenix, MSL, and LDSD projects. The peak parachute load was 55.8 klbf on SR02 and 67.4 klbf on SR03.

Following the successful deployment and inflation of the parachute, the payload and parachute descended towards the surface and splashed down into the ocean 30 minutes after launch. Post-test inspectio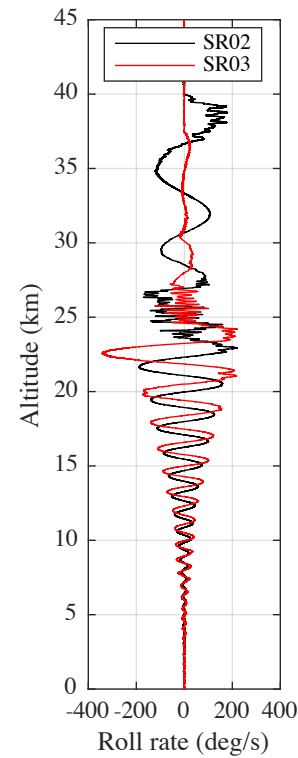n of the test articles revealed minimal damage on the SR02 canopy, and almost no damage on SR03. All instrumentation on board the vehicle functioned as expected throughout the two flights, allowing for the reconstruction of the payload trajectory, test conditions, and the performance of the test article.

It was found that the drag coefficient of the parachute was lower than expected [19] in the supersonic regime. However, the reconstructed $C_D$ of the parachute at Mach numbers below 0.75 was in excellent agreement with pre-flight predictions. The ASPIRE aerosciences team is currently exploring the discrepancy between the reconstructed supersonic $C_D$ and the pre-flight models. An effort to reconstruct the three-dimensional geometry of the canopy during inflation and supersonic flight from the HS camera footage is currently underway. This reconstruction will yield information about the inflated shape of the canopy, the location of the canopy relative to the payload, and the payload-parachute dynamics. These results may provide insight into the lower-than-expected supersonic drag. In particular, the aerosciences team is currently conducting simulations of an inflated rigid canopy in the wake of the ASPIRE and MSL vehicle using flight-like flow conditions and geometries in order to investigate the discrepancy in supersonic $C_D$. Future work will focus on investigating the dynamics of the parachute and payload during subsonic descent, using the footage from the situational awareness cameras as well as the measurements from the load pins and IMU. The objectives of this effort are to evaluate the static aerodynamic coefficients of the parachute, to investigate the dynamic aerodynamic properties of the parachute, and to characterize the system dynamics at different altitudes.
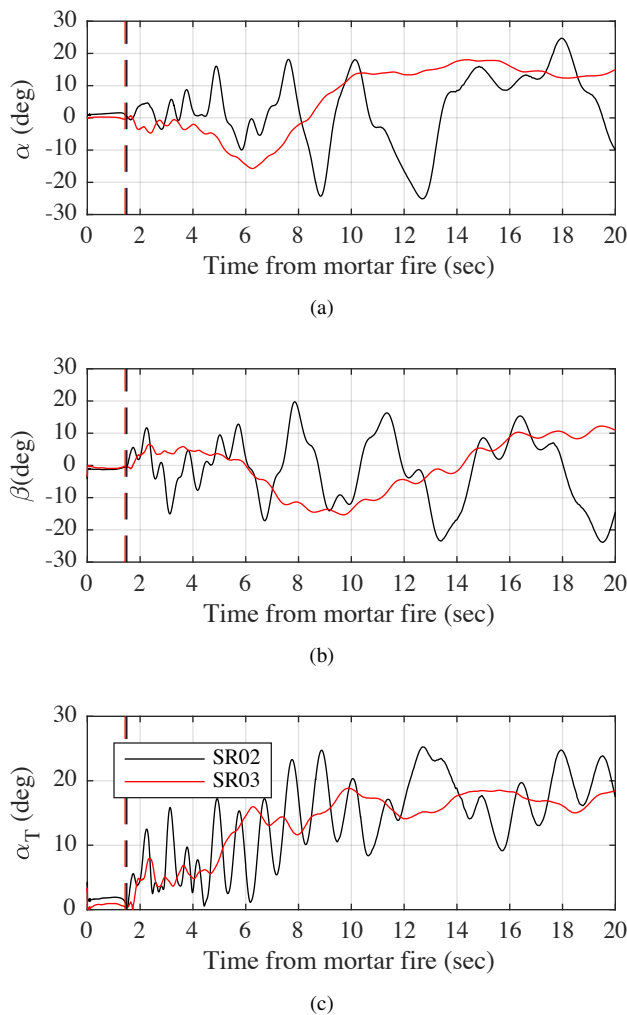
(a)



(b)



(c)

**Figure 24**. **Payload attitude during the 20 seconds following mortar fire. The dashed lines indicate the time at which peak load was achieved.**



**Figure 25**. **Minor damage to the SR02 canopy at the attachment of the bag energy modulators to the vent band.**

## REFERENCES

[1] C. G. Cooley and J. G. Lewis, "Viking 75 Project: Viking Lander System Primary Mission Performance Report," *NASA Contractor Report*, no. CR-145148, p. 118, Apr 1977.

[2] L. L. Galigher, "Aerodynamic Characteristics of Ballutes and Disk-Gap-Band Parachutes at Mach Numbers From 1.8 to 3.7," *AEDC Technical Report*, no. AEDC-TR-69-245, 1969.

[3] P. J. Bobbitt, R. J. Mayhue, G. L. Faurote, and L. L. Galigher, "Supersonic and Subsonic Wind-Tunnel Tests of Reefed and Unreefed Disk-Gap-Band Parachutes," *AIAA Paper*, no. 1970-1172, 1970.

[4] I. Jaremenko, S. Steinberg, and R. Faye-Petersen, "Scale Model Test Results of the Viking Parachute System at Mach Numbers From 0.1 Through 2.6," *NASA Contractor Report*, no. CR-149377, 1971.

[5] C. V. Eckstrom and H. N. Murrow, "Flight Tests of Cross, Modified Ringsail, and Disk-Gap- Band Parachutes from a Deployment Altitude of 3.05 km (10,000 ft)," *NASA Technical Memorandum*, no. TM X-2221, June 1971.

[6] C. V. Eckstrom and J. S. Preisser, " Flight Test of a 30-Foot-Nominal-Diameter Disk-Gap-Band Parachute Deployed at a Mach Number of 1.56 and a Dynamic Pressure of 11.4 Pounds Per Square Foot," *NASA Technical Memorandum*, no. TM X-1451, Aug 1967.

[7] J. S. Preisser and C. V. Eckstrom, "Flight Test of a 40-Foot-Nominal-Diameter Disk-Gap-Band Parachute Deployed at a Mach Number of 1.91 and a Dynamic Pressure of 11.6 Pounds Per Square Foot," *NASA Technical Memorandum*, no. TM X-1575, Aug 1968.

[8] J. S. Preisser and R. B. Grow, "High Altitude Flight Test of a Reefed 12.2-Meter Diameter Disk-Gap-Band Parachute With Deployment at a Mach Number of 2.58," *NASA Technical Memorandum*, no. TN D-6469, Aug 1971.

[9] E. J. Fallon, "System Design Overview of the Mars Pathfinder Parachute Decelerator Subsystem," *AIAA Paper*, no. 1997-1511, 1997.

[10] D. A. Spencer, R. Blanchard, R. D. Braun, P. H. Kallemeyn, and S. W. Thurman, "Mars Pathfinder Entry, Descent, and Landing Reconstruction," *Journal of Spacecraft and Rockets*, vol. 36, no. 3, pp. 357–365, May 1999.

[11] J. R. Cruz and J. S. Lingard, "Aerodynamic Decelerators for Planetary Exploration: Past, Present, and Future," *AIAA Paper*, no. 2006-6792, 2006.

[12] A. Witkowski and R. Bruno, "Mars Exploration Rover Parachute Decelerator System Program Overview," *AIAA Paper*, no. 2003-2100, 2003.

[13] D. S. Adams, A. Witkowski, and M. Kandis, "Phoenix Mars Scout Parachute Flight Behavior and Observations," *IEEE Aerospace Conference Paper*, no. 1534, 2011.

[14] J. R. Cruz, D. W. Way, J. D. Shidner, J. L. Davis, D. S. Adams, and D. S. Kipp, "Reconstruction of the Mars Science Laboratory Performance and Comparison to the Descent Simulation," *AIAA Paper*, no. 2013-1250, 2013.

[15] D. M. Kipp and D. Buecher, "A brief history of InSight parachute development and acceptance for flight," *15th International Planetary Probes Workshop*, June 2018.

[16] C. L. Tanner, I. G. Clark, and A. Chen, "Overview of the Mars 2020 Parachute Risk Reduction Plan," *IEEEAC Paper*, 2018.

[17] C. O'Farrell, C. Karlgaard, J. A. Tynis, and I. G. Clark, "Overview and Reconstruction of the ASPIRE Project's SR01 Supersonic Parachute Test," *IEEEAC Paper*, 2018.

[18] S. Dutta, E. M. Queen, A. L. Bowes, and M. C. Ivanov, "ASPIRE Flight Mechanics Modeling and Post Flight Analysis," *AIAA Atmospheric Flight Mechanics Conference*, June 2018.

[19] C. O'Farrell, S. Muppidi, J. M. Brock, J. W. Van Norman, and I. G. Clark, "Development of Models for Disk-Gap-Band Parachutes Deployed Supersonically in the Wake of a Slender Body," *IEEEAC Paper*, 2017.

[20] M. Rienecker, M. Suarez, R. Todling, J. Bacmeister, L. Takacs, H.-C. Liu, W. Gu, M. Sienkiewicz, R. Koster, R. Gelaro, I. Stajner, and J. Nielsen, "The GEOS-5 Data Assimilation System - Documentation of Versions 5.0.1, 5.1.0, and 5.2.0," *NASA Technical Memorandum*, no. 104606, 2008.

[21] G. C. Greene, "Opening Distance of a Parachute," *Journal of Spacecraft and Rockets*, vol. 7, no. 1, 1970.

[22] J. Rabinovitch, G. Griffin, W. Seto, C. O'Farrell, C. Tanner, and I. Clark, "ASPIRE Supersonic Parachute Shape Reconstruction: Experimental Results and Comparisons to Simulations," *AIAA Paper*, January 2019.

## BIOGRAPHY



*Clara O'Farrell* is an engineer in the Entry, Descent, and Landing Guidance and Control Systems Group at JPL. She received a PhD in Control and Dynamical Systems from Caltech in 2013, and a BSE in Mechanical and Aerospace Engineering from Princeton University in 2008. Since joining JPL in 2013, she has worked on the Low-Density Supersonic Decelerators and ASPIRE projects.



*Bryan S. Sonneveldt* is a Systems Engineer in the Entry, Descent, and Landing & Advanced Technologies Group at JPL. He received B.S. and M.S. degrees in Aerospace Engineering from the Arizona State University. He is a member of the ASPIRE mechanical and recovery teams, and served as the lead engineer for SR02 and SR03 post-flight reconstruction.
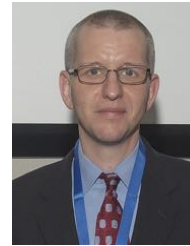


*Chris Karlgaard* received B.S. degrees in mathematics and aerospace engineering from the University of Maryland, and M.S. and Ph.D. degrees in aerospace engineering from Virginia Tech. He has been employed with Analytical Mechanics Associates, Inc. in Hampton VA since 2001, where he is currently a supervising engineer. His areas of expertise include Kalman filtering, state estimation, and flight dynamics.



*Jake A. Tynis* is an Aerospace Engineer with Analytical Mechanics Associates, Inc. in Hampton, VA. He received his B.S. and M.S. degrees in Mechanical Engineering and Aerospace Engineering from Old Dominion University. Since joining AMA in 2017, Jake has been a member of the ASPIRE and ADEPT reconstruction teams.



*Ian G. Clark* is a Systems Engineer at JPL, and a specialist in the area of Planetary Entry, Descent, and Landing (EDL). Dr. Clark is the recipient of a number of awards including the Presidential Early Career Award for Scientists and Engineers, the JPL Lew Allen Award, and the JPL Explorer Award. He was Principal Investigator of the Low-Density Supersonic Decelerators and ASPIRE projects. He holds B.S., M.S., and Ph.D. degrees in Aerospace Engineering from the Georgia Institute of Technology, where he also previously served as a Visiting Assistant Professor.